Dual-Mode Fluorescence/Ultrasound Imaging with Biocompatible Metal-Doped Graphene Quantum Dots

Alina R. Valimukhametova,

Department of Physics and Astronomy, Texas Christian University, Fort Worth, Texas 76129, United States

Olga S. Zub,

Alfa Radiology Management, Inc, Plano, Texas 75023, United States

Bong Han Lee,

Department of Physics and Astronomy, Texas Christian University, Fort Worth, Texas 76129, United States

Olivia Fannon,

Department of Physics and Astronomy, Texas Christian University, Fort Worth, Texas 76129, United States

Steven Nguyen,

Department of Physics and Astronomy, Texas Christian University, Fort Worth, Texas 76129, United States

Roberto Gonzalez-Rodriguez,

Department of Chemistry and Biochemistry, Texas Christian University, Fort Worth, Texas 76129, United States;

Giridhar R. Akkaraju,

Department of Biology, Texas Christian University, Fort Worth, Texas 76129, United States

Anton V. Naumov

Department of Physics and Astronomy, Texas Christian University, Fort Worth, Texas 76129, United States

Abstract

Corresponding Author Anton V. Naumov – *Department of Physics and Astronomy, Texas Christian University, Fort Worth, Texas 76129, United States*; a.naumov@tcu.edu.

Present Address: Department of Physics, University of North Texas, Denton, Texas, 76203, USA

Sonography offers many advantages over standard methods of diagnostic imaging due to its non-invasiveness, substantial tissue penetration depth, and low cost. The benefits of ultrasound imaging call for the development of ultrasound-trackable drug delivery vehicles that can address a variety of therapeutic targets. One disadvantage of the technique is the lack of high-precision imaging, which can be circumvented by complementing ultrasound contrast agents with visible and, especially, near-infrared (NIR) fluorophores. In this work, we, for the first time, develop a variety of lightly metal-doped (iron oxide, silver, thulium, neodymium, cerium oxide, cerium chloride, and molybdenum disulfide) nitrogen-containing graphene quantum dots (NGQDs) that demonstrate high-contrast properties in the ultrasound brightness mode and exhibit visible and/or near-infrared fluorescence imaging capabilities. NGQDs synthesized from glucosamine precursors with only a few percent metal doping do not introduce additional toxicity in vitro, yielding over 80% cell viability up to 2 mg/mL doses. Their small (<50 nm) sizes warrant effective cell internalization, while oxygen-containing surface functional groups decorating their surfaces render NGQDs water soluble and allow for the attachment of therapeutics and targeting agents. Utilizing visible and/or NIR fluorescence, we demonstrate that metal-doped NGQDs experience maximum accumulation within the HEK-293 cells 6–12 h after treatment. The successful 10-fold ultrasound signal enhancement is observed at 0.5–1.6 mg/mL for most metal-doped NGQDs in the vascular phantom, agarose gel, and animal tissue. A combination of non-invasive ultrasound imaging with capabilities of high-precision fluorescence tracking makes these metal-doped NGQDs a viable agent for a variety of theragnostic applications.

Graphical abstract
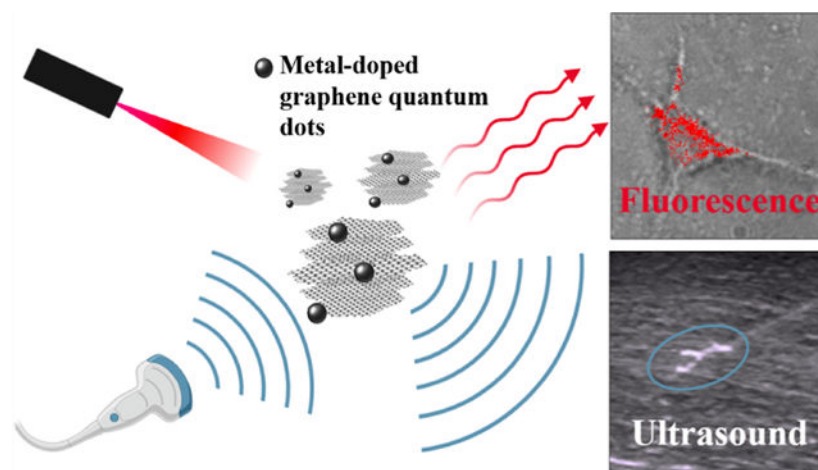
Keywords

graphene quantum dots; metal doping; ultrasound contrast agent; visible fluorescence; near-infrared fluorescence; ultrasound imaging; confocal imaging

1. INTRODUCTION

Non-invasive diagnostic methods are rapidly evolving to become promising tools in disease prevention.[1,2] Simplicity and painlessness of health checkups positively affect patients'

experience in early diagnostics, while readable clinical reported utcomes improve patient understanding of underlying diseases.[3] In remote areas of low-income regions/countries, disease prevention and early diagnostics are often insufficient, and in some instances, completely lacking.[4] For this reason, there is an apodictic need to develop simplistic, affordable methods of diagnostic imaging. Sonography can be considered affordable while possessing substantial global availability, portability, and versatility. Moreover, ultrasound systems have already been used as the means of point-of-care tests since they became more advanced, widespread, and user-friendly within the past few decades.[5,6] This is why ultrasound has gained recognition as a valuable diagnostic tool by the World Health Organization (WHO).[7] Besides being portable and low cost, sonography offers deep tissue penetration up to 22 cm at low-frequency settings[8] and, in certain specific cases, can achieve substantial spatial (0.1 mm at 15 MHz) and temporal resolutions, providing real-time feedback.[9]

Typical diagnostic sonographic scanners operate in the frequency range of 2–18 MHz, orders of magnitude above the limit of human hearing, ensuring comfort and usability for patients. Medical ultrasound is based on the ability to differentiate between the internal organs and their compartments from surrounding tissue due to their different acoustic impedance.[10] However, when diagnostic targets cannot be distinguished from the surrounding tissue, contrast-enhanced ultrasound (CEUS) may enable more specific detection. CEUS is an established technique in cardiac imaging,[11] as well as in the visualization of liver lesions[12] and renal carcinoma diagnostics.[13] The present-day ultrasound contrast agents (UCAs) have to satisfy the following requirements: (1) be biocompatible and biodegradable, (2) have high stability in blood, and (3) have good echogenicity (ability to reflect an ultrasound signal). Currently, there are three FDA-approved UCAs: Lumason (Bracco, Milan, Italy), Definity (Lantheus, North Billerica, MA, USA), and Optison (GE Healthcare, Oslo, Norway) that generally satisfy the aforementioned conditions. These contrast agents consist of inner gaseous cores surrounded by lipid or albumin micrometer-sized shells. The distinct advantage of such microbubble contrast agents over their CT and MRI counterparts is their high biocompatibility. For instance, while patients with preexisting renal conditions are known to develop adverse reactions to CT and MRI contrast agents including kidney dysfunction,[14–16] UCAs show little to no toxicity.[17] Along with all the benefits of using microbubbles as UCAs, there are some disadvantages: microbubbles do not last very long in circulation and, similarly to liposomes, can be taken up by Kupffer cells or dissociated in the blood stream.[18] They can collapse at low ultrasound frequencies and higher powers (>1.3 mechanical indices[19]), leading to local microvascular ruptures.[20] Ultrasound imaging is also limited in its resolution and is not highly applicable for high-precision targets.[21,22] Finally, these agents only enable a single diagnostic application. Given the appeal of modern therapeutics toward multimodal approaches, there is a high expectation of making ultrasound contrast agents capable of more than one function. Some of these critical issues can be addressed via advances in modern nano-biotechnology.

The main advantage of applying nanotechnology in medicine is the versatility of nanomaterials that may offer drug delivery, targeting, and detection capabilities.[23–27] Carbon-based nanomaterials often appear at the forefront of these applications.[28,29] The recent focus of carbon nanotechnology is geared toward graphene quantum dots (GQDs),

composed of several layers of graphitic carbon with lateral sizes ~10 nm. GQDs have attracted a significant interest in various biomedical applications due to their small size, structure, high biocompatibility, and optical properties.[30,31] For instance, modification of GQDs with ligands binding to specific receptors of interest can allow GQDs to accumulate selectively in the areas of interest.[32–34] GQDs may also serve as effective fluorophores due to the tunability and photostability of their fluorescence, which is utilized in vitro and in vivo.[35–37] Along with bioimaging, GQDs can provide therapeutic capabilities. For instance, folic acid-functionalized GQDs loaded with IR780 iodide can trigger HeLa cell death by photothermal effect.[38] GQD intrinsic fluorescence has been beneficially combined with other bioimaging methods, such as MRI and photoacoustic imaging (PAI), giving rise to new dual-mode contrast agents. Su et al. developed GQDs attached to the $Fe_3O_4@SiO_2$ core/shell structure and demonstrated in vitro MRI and fluorescence imaging of living Hela cells.[39] Dual-mode fluorescence/PAI was demonstrated using GQDs synthesized from citric acid. These GQDs successfully exhibit visible and near-infrared fluorescence and have the ability to also exhibit a photoacoustic response at the same time.[40] Given these advances, there is a promise of utilizing GQDs and their fluorescence as a theragnostic tool in dual-mode bioimaging combined with a variety of techniques.

Highly biocompatible and biodegradable nitrogen-containing graphene quantum dots (NGQDs) developed in our previous work[41–43] can serve as a basis for the new dual-mode contrast agent design. NGQDs exhibit fluorescence in the visible (VIS) and near-infrared (NIR) regions. They possess a substantial surface area for functionalization, where ligands can be attached non-covalently to a graphene platform or covalently to a variety of oxygen-containing functional groups.[34] These groups are protonated/deprotonated depending on the pH of the biological environment, causing a change in NGQDs' fluorescence, which is utilized in biosensing of lower pH cancerous environments.[43,44] Other sensing capabilities of these nanomaterials include miRNA and ssDNA detection, which could be utilized for cancer diagnosis.[45,46] Finally, our previous studies warrant that NGQDs can be utilized not only as imaging agents but also as successful drug delivery vehicles. For instance, the covalent attachment of ferrocene to NGQDs facilitates its enhanced delivery inside the cells and improves its redox-based cancer therapeutic effect in HeLa cells.[34]

Due to the lack of ultrasound scattering centers, NGQDs are not expected to exhibit substantial echogenicity; however, in several reports, larger carbon nanotubes and graphene oxide show enhancement of ultrasound contrast.[47,48] Functionalized multiwall carbon nanotubes (MWCNTs) used as UCAs enable increased ultrasound signals comparable to commercial UCAs and exhibit high echogenic properties in animal tissue.[48] Inorganic and metal nanoparticles can demonstrate even more substantial enhancement of ultrasound contrast at relatively smaller sizes.[49] For example, silica nanoparticles have been shown to be successfully exploited as ultrasound contrast agents in B-mode based on the structure and amount of scattering/reflection interfaces.[50–54] To further improve the ultrasound response, silicon nano/microparticles are filled with perfluoropentane[55] or air.[56] In another example, inorganic manganese dioxide encapsulated into indocyanine green nanoparticles is able to improve ultrasound scattering due to the reaction with hydrogen peroxide and the generation of oxygen.[57] Gold nanoparticles with a density different from the biological tissue can also serve as ultrasound scattering centers and, thus, perform well as contrast agents.[58]

Introduced on their own, metal nanoparticles may encounter substantial biocompatibility barriers. In order to employ advantageous properties of biocompatible NGQDs and render them suitable as UCAs, we developed a variety of lightly metal-doped NGQD structures: iron oxide nanoparticles, silver nanoparticles, thulium, neodymium, cerium oxide, cerium chloride, and molybdenum disulfide-doped NGQDs. Intrinsic fluorescence properties of NGQDs can also enhance the imaging capabilities of these UCAs. While the ultrasound resolution is limited, fluorescence allows substantially higher precision imaging, enabling tracing therapeutic delivery and detection in microscopic tissue compartments.[42,59,60] This could enable utilizing the proposed UCAs as drug delivery vehicles and microscopic environmental sensors. Their general location could be assessed by deeper tissue ultrasound imaging, while microscopic internalization dynamics and characteristics of the environment such as pH[43] or the presence of free radicals could be evaluated via their fluorescence emission and spectral signatures. Fluorescence in the visible region has limited tissue penetration depth due to high scattering, absorption, and autofluorescence, confining these applications to in vitro and ex vivo studies mostly. However, NIR fluorophores in the first and second biological windows partially escape those limitations.[60,61] In fact, a number of near-infrared fluorophores have been used for animal imaging to date including single-walled carbon nanotubes,[62] indocyanine green,[60] and gold nanoparticles.[63] Fluorescence emission from Tm- and Nd-doped NGQDs was previously observed from the organs of a live mouse[42] allowing for medium-depth fluorescence imaging. Combined high precision and sensitivity of such fluorescence imaging with deep tissue capabilities of the ultrasound could turn metal-doped NGQDs into a versatile theragnostic tool. The goal of this work is to test the ultrasound contrast and fluorescence imaging properties of a variety of metal-doped NGQD nanostructures in cells and tissues to assess their advantages over the existing agents and explore their multifunctionality. Development and utilization of such multimodal ultrasound contrast and fluorescence imaging agents can synergistically enhance detection capabilities in cells and tissues, allow for tracing therapeutic delivery, and enable establishing the early diagnosis in a cost-effective approach.

2. MATERIALS AND METHODS

2.1. Synthesis.

NGQDs: 4 g of glucosamine hydrochloride (Sigma-Aldrich batch #104K0082) was dispersed in 250 mL of deionized (DI) water and processed in the microwave oven (Hamilton Beach, model: HB-P90D23AP-ST) for 50–70 min at a 1350 W power level to produce non-doped NGQDs.

$CeCl_3$-NGQDs and CeO_2-NGQDs: in a standard procedure, 4 g of glucosamine hydrochloride (Sigma-Aldrich batch #104K0082) and either 0.3 g of $CeCl_3$ (429406, Sigma-Aldrich) or 0.35 g of CeO_2 (202975, Sigma-Aldrich) were dispersed in 250 mL of deionized (DI) water and processed in the microwave oven for 50–70 min at a 1350 W power level to produce $CeCl_2$-NGQDs or CeO_2-NGQDs.

Nd-NGQDs and Tm-NGQDs were synthesized following the procedure in our previous work.[42]

Silver nanoparticle-NGQDs (silver NP-GQDs): 10 ml of silver NPs and 4 g of glucosamine hydrochloride (Sigma-Aldrich batch #104K0082) were added to 250 mL of DI water and processed in the microwave oven for 50–70 min at a 1350 W power level to produce silver NP-NGQDs. The weight ratio of C/Ag is 208.

Iron oxide nanoparticle-GQDs (iron oxide NP-NGQDs): 1 mL of iron oxide nanoparticle water dispersion (15 wt % in water, Fe_2O_3 Alpha, 99.9%, 5 nm; US Research Nanomaterials, Inc) was added to 14 mL of DI water. The mixture was directly probe-sonicated (Qsonica Q55 Sonicator Ultrasonic Homogenizer with Probe 55 W, 30% amplitude) for 1 min, added to 4 g of glucosamine hydrochloride (Sigma-Aldrich batch #104K0082), and dispersed in 225 mL of DI water. The suspension was further processed in the microwave oven for 50–70 min at a 1350 W power level to produce iron oxide NP-NGQDs.

MoS_2-NGQDs: 7 mg of MoS_2 (69860, Sigma-Aldrich) dispersed in 10 mL of DI water and 7 mg of SDS (151-21-3, Alfa Aesar) dispersed in the other 10 mL of DI water were mixed and vortexed together for 30 s and processed using an ultrasonic tip sonicator (Qsonica Q55 Sonicator Ultrasonic Homogenizer with Probe 55 W, 30% amplitude) for 30 min. The suspension was left overnight, and the suspended supernatant was used as a stock. 0.625 g of glucosamine hydrochloride (Sigma-Aldrich batch #104K0082) and 20 mL of stock MoS_2 were added to 150 mL of DI water. The mixture was vortexed for 1 min and processed in the microwave oven for 50–70 min at a 1350 W power level to produce MoS_2-NGQDs.

During the microwave treatment, temperatures reached the boiling point of the suspension; however, the product remained dissolved in water throughout the process. After the synthesis, samples are transferred to a 10 kDa molecular weight cutoff (MWCO) bag to remove the unreacted precursors via dialysis for 24 h against DI water. The water was changed every 30 min for the first 3 h, after which it was changed every 7 h. Purified materials were further filtered through the 0.22 μm syringe filter in order to remove any aggregates that occurred in the prior dialysis procedure and sterilize the product. The dialyzed and filtered product remained and was further used in the suspension form.

2.2. Structural/Optical Characterization (FTIR, Absorbance, Fluorescence, Raman, HRTEM/TEM, and EDS).

To assess the functional groups of metal-doped NGQDs, the samples were freeze-dried in the Labconco FreeZone 4.5 freeze-dryer and analyzed via the ATR mode of the Thermo Nicolet Nexus 670 FTIR. The absorbance of metal-doped NGQDs was measured within the range of 200–1000 nm using the Agilent Technologies (Cary 60 UV–vis) absorption spectrometer. The fluorescence and PLE maps in the visible region were recorded using Horiba Scientific's SPEX NanoLog fluorescence spectrofluorometer. In PLE experiments, the excitation wavelength was scanned from 375 to 465 nm at 4 nm intervals. The fluorescence in the NIR region was measured using an 808 nm excitation laser and the AvaSpec-HS TEC SensLine spectrometer from Avantes Inc. Fluorescence microscopy was performed using an Olympus IX73 fluorescence microscope with a 60× (IR-corrected Olympus Plan Apo) water immersion objective. The microscope is coupled to the NIR InGaAs Photon etc. (ZephIR 1.7) detector thermoelectrically cooled to −80 °C through the

hyperspectral fluorescence imager (Photon etc.), enabling spectrally resolved imaging in the near-infrared region (850–1600 nm). The morphological characterization of the metal-doped NGQDs was performed by HRTEM (high-resolution transmission electron microscopy, JEOL JEM-2100) with energy dispersive X-ray analysis (EDS, JEOL, Peabody, MA, USA). For the TEM measurements, the samples were freeze-dried (Labconco, FreeZone 4.5 freeze-dryer) on the carbon-coated 200-mesh copper grid.

2.3. Cell Culture.

In vitro studies were performed using human embryonic kidney 293 (HEK-293) cells. The cells were cultured in Dulbecco's modified Eagle medium (D6046, Sigma-Aldrich), 10% fetal bovine serum (16140–063, Gibco), L-glutamine (G7513, Sigma-Aldrich), minimum essential medium non-essential amino acid solution (M7145, Sigma-Aldrich), and 1% penicillin/streptomycin (P4333, Sigma-Aldrich). The cell culture was placed in a Midi 40 CO_2 incubator (3403, Thermo Scientific) at 37 °C with 5% CO_2 and further utilized for the cell viability assay as well as the cell internalization study.

2.4. MTT Assays.

Standard MTT cell viability assays were employed to evaluate the cytotoxicity of metal-doped NGQDs. HeLa cells were plated in a 96-well plate at a density of 5000 cells per well (100 μL per well) and kept in an incubator overnight at 37.1 °C while maintaining 5% CO_2. After 24 h of incubation, the samples were added into each well in serial dilutions. After the next 24 h (24 h and 48 h for non-doped NGQDs) of incubation, the medium was replaced by 100 μL of 1 mg/mL of thiazolyl blue tetrazolium bromide. After 4 h of further incubation, MTT (3-(4-dimethylthiazol-2-yl)-2,5-diphenyltetrazolium bromide) was replaced with 100 μL of dimethyl sulfoxide (DMSO) to solubilize a highly absorbing byproduct known as formazan. The metabolic activity of living cells was further assessed with absorbance measurements. The absorbance of formazan proportional to cell viability was measured in each well at 580 nm using a FLUOstar Omega microplate reader.

2.5. Cell Internalization Study.

The cell internalization study was performed with 1 mg/mL of metal-doped NGQDs' concentrations. A total of 10,000 cells have been seeded onto coverslips placed in a six-well plate. The coverslips have been sterilized and coated with rat tail collagen I (ALX-522-435-0020, Enzo) for the attachment of HEK-293 cells. After the cells showed adherence to the coverslips, metal-doped NGQD samples were introduced in cell growth medium and incubated for 1, 6, 12, 24, and 48 h. Coverslips with cells were then washed with 1X phosphate-buffered saline (PBS) to remove NGQDs that had not been internalized. Cells were further fixed with 4% formaldehyde solution (28908, Thermo Scientific) and 1× Fluoromount-GTM mounting medium (00-4958-02, Invitrogen) to be later sealed onto microscope slides. At each time point, ~200 cells were imaged and the mean fluorescence intensity per unit area was calculated for each cell.

2.6.   Ultrasound Imaging.

All ultrasound imaging was performed with the GE Logiq e ultrasound system. The instrument was set in the B-mode and CHI mode, with a depth of 4–5 cm, mechanical index of 0.5–0.6, and gain of 44–66. The transducer was coated with Aquasonic 100 ultrasound transmission gel. Water dispersions of metal-doped NGQDs in the concentrations range of 0.5 to 1.6 mg/mL are injected with a 10 mL syringe and imaged in a vascular phantom (Ultrasound Guided IV Trainer, Your Design Medical), 2% agarose gel block, and chicken breast tissue. Experiments were performed using a 10–13 MHz linear probe placed perpendicularly to the observed object. The ultrasound signals on the bar plots are reported in 8-bit gray scale intensity from 0 to 255 shades of gray. Ultrasound images were further analyzed using ImageJ to assess the signal intensity arising from NGQDs. Statistical analysis on three samples was performed using one-way ANOVA analysis.

3.   RESULTS AND DISCUSSION

$CeCl_3$-NGQDs, CeO_2-NGQDs, Nd-NGQDs, Tm-NGQDs, silver NP-NGQDs, iron oxide NP-NGQDs, and MoS_2-NGQDs are prepared in this work using a microwave-assisted hydrothermal synthetic approach[41] with glucosamine as the carbon precursor. Upon microwave treatment, glucosamine molecules undergo dehydration reaction that leads to their polymerization. Such structures serve as nucleation centers for the formation of NGQDs. At the same time, metal salts or oxides serve as dopant donors, introducing metal atoms into nucleating NGQDs. Several characterization methods are utilized to confirm and assess the physical as well as optical properties of the synthesized nanomaterials. After purification and sterilization, all metal-doped NGQDs are imaged by TEM to confirm their graphitic structure and assess their size distribution (Figure S1). With distribution means varying from 1.6 ± 0.7 nm for silver NP-NGQDs to 23.2 ± 9.3 nm for CeO_2-NGQDs, the sizes of synthesized NGQDs do not exceed 50 nm, allowing their cellular internalization via clathrin-mediated endocytosis.[64] Additionally, HRTEM images (Figure 1) demonstrate characteristic lattice fringes of the graphitic structure of NGQDs, and the fast Fourier transform (FFT) of the HRTEM images allows us to ensure the crystallinity of individual metal-doped NGQDs on the nanoscale. The interplanar distance measurements for all seven NGQD types range between 0.22 and 0.28 nm, likely corresponding to the (100) plane of graphene. The presence of the sp^2 graphitic lattice suggests a potential application of this material for drug and oligonucleotide delivery via their non-covalent π–π stacking onto the NGQD graphitic surface.[65,66] Due to the layered structure of MoS_2, TEM images of MoS_2-NGQDs (Figure 1) also show fringes with an interplanar distance of 1.04 ± 0.08 nm, corresponding to the interlayer expanded MoS_2.[67] As evident from EDX analysis, MoS_2 and NGQDs form a joint structure (Figure S2), meaning their crystal structures are rather embedded than spatially separated.

The EDX analysis demonstrates the presence of expected metal dopants in each sample (Table 1, Figure S2). A purification filtration step ensures that dopants are bound within the NGQD structure as all the water-soluble metal salts are dialyzed out. Doping with metals and metal oxides in this reaction generally does not exceed 1%, suggesting that it may not affect the biocompatibility of the synthesized material. Although the amount of cerium

in CeCl$_3$-NGQDs is greater (~5%), these NGQDs are still not expected to possess high toxicity due to cerium being reportedly highly biocompatible.[68,69] Besides the metals, all samples mostly contain carbon and small amounts of nitrogen and oxygen similar to those in non-doped NGQDs. The presence of these elements suggests that NGQDs possess a carbon-based structure with functional groups on their surface that render NGQDs water soluble. FTIR analysis (Figure S3) performed on all samples shows identical spectral features, corresponding to hydroxyl, carboxyl, and, likely, amino groups arising from a common glucosamine precursor.[41]

Absorbance and fluorescence spectroscopies are utilized to assess the optical properties of the synthesized metal-doped NGQDs and evaluate their potential for fluorescence imaging in the visible and near-infrared regions. All NGQDs exhibit similar general absorption features (Figure S4a) including n–π* electronic transitions of C═O at ~283 nm[70] and a shoulder from π–π* transitions ascribed to C═N groups at ~317 nm.[71] These features also verify the presence of the corresponding functional groups on the NGQDs' surface. The absorption peak at 230 nm is attributed to the π–π* transition of aromatic C═C bonds in NGQD graphitic regions.[70] Other dopant-specific features indicate successful doping with several metals. MoS$_2$-NGQDs display a peak at 250 nm that can be related to the excitonic features of nanolayered MoS$_2$.[72] Tm-NGQDs and Nd-NGQDs have absorption peaks in the NIR range (Figure S4b), corresponding to the $^4I_{9/2} \rightarrow {}^4F_{5/2}$ transition for Nd-NGQDs and the $^3H_6 \rightarrow {}^3H_4$ transition for Tm-NGQDs.[42] These transitions enable fluorescence excitation in the NIR region, allowing excitation light to penetrate deeper into biological tissue,[73] thus, providing potential for deeper tissue imaging. In our previous work, we showed that Nd- and Tm-NGQDs indeed exhibit NIR fluorescence in vitro/in vivo/ex vivo with 808 nm laser excitation. These capabilities warranted by the NIR excitation and emission at both 1060 nm and ~950 nm (Figure S5) make them promising candidates for fluorescence diagnostic imaging in vivo.

All NGQD samples exhibit fluorescence in the visible range (Figure 2a), which is generally comparable to the emission of their non-doped counterparts,[74] indicating that the doping did not affect their optical properties in the visible region. This behavior is expected as the optical properties of graphene derivatives have less dependence on the type of functionalization and are mostly manifested by the size of the graphitic island[75,76] entrapped by functional groups. Only the iron oxide NP-NGQDs demonstrate a fluorescence shift and more pronounced excitation dependence (Figure 2b), potentially due to charge transfer from iron oxide nanoparticles.[77] Similar shifts are observed for graphene oxide doped with iron oxide nanoparticles.[78] PLE maps (Figures 2b–d and S6) of metal-doped NGQDs help assess the optimal wavelengths of excitation/emission to use for fluorescence microscopy imaging with these nanomaterials in the visible region.

Following the confirmation of doped NGQDs' optical properties, they are utilized for in vitro studies to assess their capabilities as fluorescence imaging agents. First, the biocompatibility of those metal-doped NGQDs is evaluated to determine the concentration that does not prohibit NGQDs from biological applications. Cell viability MTT assays performed in non-cancerous HEK-293 cells (Figure 3) demonstrate that over 80% cell viability is achieved at high concentrations of up to 2 mg/ml for most NGQDs. Such high

biocompatibility comparable to that of non-doped NGQDs[43] (Figure S7) suggests that light metal doping did not substantially affect their biological properties. Cell viability appears to be high and stable after 24 and 48 h of treatment by non-doped NGQDs (Figure S7). Based on this result, we expect metal-doped NGQDs to yield similar cell viability after 48 h treatment. MoS_2-NGQDs demonstrate substantial toxicity at low concentrations and thus show 80% cell viability only at 0.05 mg/mL. This toxicity is expected since MoS_2 sheets composing part of MoS_2-NGQDs are known to be somewhat more toxic.[79] Cell viability over 100% at smaller concentrations for a number of NGQD structures can arise from the degradation of NGQDs and digestion of the organic glucose-based structures by the cells as observed in previous work.[34,43] In light of this demonstrated biocompatibility at such high concentrations, synthesized metal-doped NGQDs justify their potential for applications for bioimaging and therapeutic delivery.

One of the main hypotheses of this work is the application of metal-doped NGQDs for fluorescence imaging. Previously, we have reported the stability of NGQDs, demonstrating that the fluorescence of NGQDs did not decline for several hours with prolonged irradiation.[41,43] The stability of the ferrocene-NGQDs–hyaluronic acid complex in multiple media, including cell medium and mouse blood serum, lasts within 48 h based on their fluorescence.[34] In order to track metal-doped NGQDs inside the cells and assess the optimal timeline for imaging, a fluorescence-based internalization/excretion study is performed via in vitro fluorescence microscopy. Based on the NGQD optical properties, visible fluorescence emission within the cells is recorded with 460 nm filtered lamp excitation and 540 nm filtered emission. All samples are introduced into the HEK-293 cells and incubated for 1, 6, 12, 24, and 48 h. The fluorescence intensity per cell area is used as a measure of internalization/excretion dynamics of the nanomaterial in the HEK-293 cells over time (Figure 4). Such imaging accounts only for the NGQDs that internalize, since the ones remaining in the intracellular space are removed by a washing step during slide preparation. Examples of overlay bright-field/fluorescence images of all samples at different time points (Table S1) show successful internalization of all the NGQDs within 12 h timeframe. In order to quantify the internalization, the NGQD emission from over 200 cells is analyzed at each time point for each NGQD type, and the average intensity per unit cell area is then used as a measure of the intercellular NGQD concentration. This analysis (Figure 4a,b) demonstrates that silver NP-NGQDs, Nd-NGQDs, Tm-NGQDs, $CeCl_3$-NGQDs, iron oxide NP-NGQDs, CeO_2-NGQDs, and MoS_2-NGQDs experience maximum accumulation 6–12 h after treatment. The decrease in the fluorescence signal from cells after these time points suggests the excretion of NGQDs.

Confocal fluorescence microscopy of the median plane of cells allows observing metal-doped NGQDs that have been internalized inside the cell, disregarding the NGQDs only attached to the membrane (Figure 5a). Bright-field/VIS fluorescence confocal cell image overlays (Figure 5a) verify the successful internalization and stable fluorescence of all metal-doped NGQDs inside the cells at 6 or 12 h of the optimal imaging time point. Visible fluorescence inside the cells demonstrates that metal-doped NGQDs can serve as an intracellular therapeutic tracking agent. Additionally, Tm-NGQDs and Nd-NGQDs exhibit fluorescence in the NIR (Figure 5b), confirming their potential for in vivo imaging. Their spectral signatures collected from the emissive regions within the cell via hyperspectral

microscopy correspond to the emission spectra of Nd- and Tm-NGQDs measured in aqueous suspension (Figure S5). This verifies the presence of these metal-doped NGQDs within the cells.

In order to assess the capabilities of all fluorescent NGQDs to enhance ultrasound imaging, NGQD samples at biocompatible concentrations ranging from 0.5 to 1.6 mg/mL are tested in three biological tissue-simulating environments. First, aqueous suspensions of metal-doped NGQDs are introduced inside the vascular phantom in gel casing (Figure 6), with non-doped NGQDs and DI water used as controls. While both controls (Figures 6 and S8) injected in the vascular phantom channels show nearly no signal in the ultrasound, metal-doped NGQDs exhibit substantial scattering and, thus, provide ultrasound contrast as they move through the channels (Figure 6). Ultrasound intensity from the metal-doped NGQDs in the vascular phantom is comparable to hollow silicon nanoparticles at 1 mg/mL[54] and oxidized single-wall carbon nanotubes at 1 mg/mL[48] tested in vitro. Image analyses of metal-doped and non-doped NGQDs yield statistically significant difference ($P < 0.05$), indicating that all metal-doped and non-doped NGQDs are echogenic as compared to the control water, although metal-doped NGQDs demonstrate around 10 times higher intensity. To investigate their ultrasound contrast capability in different density materials simulating different types of human tissue, metal-doped NGQDs are injected and imaged in chicken breast (1.15 g/cm^3) (Figure 6) and 2% agarose gel (1.008 g/cm^3) (Figure S9). Long thick and short thin white lines in Figure 6 correspond to the epimysium and perimysium of a muscle, respectively. An epimysium is the sheath of tissue surrounding a muscle, while a perimysium is the sheath of tissue surrounding a bundle of muscle fibers. Due to their thicker structures, they are both echogenic and appear in a normal ultrasound image of the tissue.[80] White lines and dots in Figure S9 represent artifacts of agarose gel, corresponding to the inhomogeneous structure and air bubbles trapped during gel solidification. As a result, a majority of samples demonstrate a high ultrasound response in the place of injection, indicating their ultrasound contrast capabilities. Water controls again show no substantial contrast enhancement. Silver NP-NGQDs, iron oxide NP-NGQDs, Nd-NGQDs, Tm-NGQDs, CeO_2-NGQDs, and MoS_2-NGQDs injected into the chicken breast exhibit higher ultrasound contrast than the oxidized MWCNT at 1 mg/mL tested in the pig's liver and heart.[48] It is also apparent that $CeCl_3$-NGQDs show lower contrast at a biocompatible concentration after injection into the chicken breast and only exhibit substantial ultrasound enhancement at higher doses (Figure S8). Silver NP-NGQDs, iron oxide NP-NGQDs, Nd-NGQDs, Tm-NGQDs, CeO_2-NGQDs, and MoS_2-NGQDs can therefore carry a promising potential for vascular imaging and tissue imaging. The lack of ultrasound enhancement from the NGQDs without any dopants (NGQDs) suggests that even a small metal doping percentage results in substantial scattering. All metal-doped NGQDs were tested using a 10–13 MHz linear probe, making them beneficial for bioimaging comparable to commercial microbubbles that tend to rupture at these frequencies.[81] Currently, there are no papers known to the authors that discuss the ultrasound contrast properties of GQDs. Due to the higher acoustic impedance of graphene[82] as compared to biological soft tissue, graphene derivatives such as NGQDs or multiwalled nanotubes are expected to exhibit some echogenicity. In our work, metal doping further enhances that effect without substantial detriment to NGQD biocompatibility. It is likely that the features observed in vascular

phantom sonograms (Figure 6) are not a result of individual QD scattering but can rather be attributed to loose aggregates or groups of NGQDs injected into the channel. It is also unexpected that $CeCl_3$-NGQDs, having the most metal doping, demonstrate only weak echogenic properties in tissue. This may suggest that the mechanism of contrast formation is more complex than just acoustic scattering, with a potential dependence on metal distribution throughout the NGQDs or microscopic air bubble trapping at the dopant/defect sites.[83–85] This provides grounds for investigation in future work involving varying doping percentages. Following the major hypothesis of this work, metal-doped NGQDs successfully show both ultrasound contrast and fluorescence imaging capabilities and, therefore, can be considered promising novel candidates for complementary dual-mode ultrasound and fluorescence imaging.

4. CONCLUSIONS

In this work, lightly metal-doped nitrogen-containing GQDs including silver NP-NGQDs, Nd-NGQDs, Tm-NGQDs, $CeCl_3$-NGQDs, iron oxide NP-NGQDs, CeO_2-NGQDs, and MoS_2-NGQDs are assessed for dual-mode fluorescence and ultrasound imaging capabilities in vitro and in tissue phantoms. These NGQDs are synthesized via a cost-effective and scalable hydrothermal microwave-assisted method with a single glucosamine precursor and the addition of the corresponding metal salts/oxides. Having a small size (<50 nm), all NGQDs successfully internalize into HEK-293 cells with maximum accumulation times of 6 to 12 h. Within the cells, all seven metal-doped NGQD types exhibit visible (while Tm and Nd-NGQDs also show near-infrared) fluorescence, allowing for extra- and intra-cellular tracking. Near-infrared fluorescence possesses the additional advantage of a higher penetration depth for fluorescence imaging in biological organs and tissues. Due to only light metal doping (<5%), silver NP-NGQDs, Nd-NGQDs, Tm-NGQDs, $CeCl_3$-NGQDs, iron oxide NP-NGQDs, and CeO_2-NGQDs demonstrate biocompatibility at high concentrations of up to 2 mg/mL, making those NGQDs prospective candidates for biological applications. Their ultrasound contrast imaging modality is verified by acoustic sonography experiments in vascular phantoms and biological tissue phantoms similar in density and/or structure to soft tissue. Silver NP-NGQDs, Nd-GQDs, Tm-GQDs, iron oxide NP-NGQDs, CeO_2-NGQDs, and MoS_2-NGQDs show 10-fold higher ultrasound contrast within the vascular phantom, agarose gel, and chicken breast tissue in the ultrasound brightness mode compared to non-doped NGQDs and DI water. That suggests that metal dopants play an essential role in ultrasound contrast generation even though density-based ultrasound scattering may not be the only mechanism driving such a response. Overall, lightly metal-doped NGQDs demonstrate high potential as both ultrasound contrast and visible and/or near-infrared fluorescence imaging agents. Having two imaging modalities complementing each other in high penetration depth (ultrasound) and specificity/precision (fluorescence) makes NGQDs a powerful theragnostic platform for imaging, sensing, or drug delivery.

Supplementary Material

Refer to Web version on PubMed Central for supplementary material.

Author Manuscript

ACKNOWLEDGMENTS

REFERENCES

(1). Hiom S. Diagnosing cancer earlier: reviewing the evidence for improving cancer survival. Br. J. Cancer 2015, 112, S1–S5. [PubMed: 25734391]

(2). Tørring ML; Frydenberg M; Hansen RP; Olesen F; Vedsted P. Evidence of increasing mortality with longer diagnostic intervals for five common cancers: a cohort study in primary care. Eur. J. Cancer 2013, 49, 2187–2198. [PubMed: 23453935]

(3). McKay A; Pantoja C; Hall R; Matthews S; Spalding P; Banerjee R. Patient understanding and experience of non-invasive imaging diagnostic techniques and the liver patient pathway. J. Patient-Rep. Outcomes 2021, 5, 89. [PubMed: 34508298]

(4). Yadav H; Shah D; Sayed S; Horton S; Schroeder LF. Availability of essential diagnostics in ten low-income and middle-income countries: results from national health facility surveys. Lancet Global Health 2021, 9, e1553–e1560. [PubMed: 34626546]

(5). Moore CL; Copel JA. Point-of-care ultrasonography. N. Engl.J. Med 2011, 364, 749–757. [PubMed: 21345104]

(6). Weile J; Brix J; Moellekaer AB. Is point-of-care ultrasound disruptive innovation? Formulating why POCUS is different from conventional comprehensive ultrasound. Crit. Ultrasound J 2018, 10, 25. [PubMed: 30270416]

(7). Buscarini E; Lutz H; Mirk P; Organization WH Manual of Diagnostic Ultrasound; World Health Organization, 2013.

(8). Alter K; Skurow S Instrumentation and knobology. Ultrasound Guided Chemodenervation Procedures; Springer, 2012; pp 84–107.

(9). van Randen A; Laméris W; Laméris HW; van Es HP; van Heesewijk B; van Ramshorst W; ten Hove WH; Bouma MS; van Leeuwen EM; van Keulen PM; Bossuyt PM; Stoker J; Boermeester MA. A comparison of the accuracy of ultrasound and computed tomography in common diagnoses causing acute abdominal pain. Eur. Radiol 2011, 21, 1535–1545. [PubMed: 21365197]

(10). Powles AE; Martin DJ; Wells IT; Goodwin CR. Physics of ultrasound. Anaesth. Intensive Care Med 2018, 19, 202–205.

(11). Porter TR; Abdelmoneim S; Belcik JT; McCulloch ML; Mulvagh SL; Olson JJ; Porcelli C; Tsutsui JM; Wei K. Guidelines for the cardiac sonographer in the performance of contrast echocardiography: a focused update from the American Society of Echocardiography. J. Am. Soc. Echocardiogr 2014, 27, 797–810. [PubMed: 25085408]

(12). Dietrich CF; Nolsøe CP; Barr RG; Berzigotti A; Burns PN; Cantisani V; Chammas MC; Chaubal N; Choi BI; Clevert D-A; Cui X; Dong Y; D'Onofrio M; Fowlkes JB; Gilja OH; Huang P; Ignee A; Jenssen C; Kono Y; Kudo M; Lassau N; Lee WJ; Lee JY; Liang P; Lim A; Lyshchik A; Meloni MF; Correas JM; Minami Y; Moriyasu F; Nicolau C; Piscaglia F; Saftoiu A; Sidhu PS; Sporea I; Torzilli G; Xie X; Zheng R. Guidelines and good clinical practice recommendations for contrast enhanced ultrasound (CEUS) in the liver–update 2020–WFUMB in cooperation with EFSUMB, AFSUMB, AIUM, and FLAUS. Eur. J. Ultrasound 2020, 41, 562–585.

(13). Dong X.-q.; Shen Y; Xu L.-w.; Xu C.-m.; Bi W; Wang X.-m. Contrast-enhanced ultrasound for detection and diagnosis of renal clear cell carcinoma. Chin. Med. J 2009, 122, 1179–1183. [PubMed: 19493467]

(14). Andreucci M; Faga T; Pisani A; Sabbatini M; Michael A. Acute kidney injury by radiographic contrast media: pathogenesis and prevention. BioMed Res. Int 2014, 2014. DOI: 10.1155/2014/362725

(15). Hasebroock KM; Serkova NJ. Toxicity of MRI and CT contrast agents. Expet Opin. Drug Metabol. Toxicol 2009, 5, 403–416.

(16). ter Haar G. Safety and bio-effects of ultrasound contrast agents. Med. Biol. Eng. Comput 2009, 47, 893–900. [PubMed: 19597745]

(17). Kalantarinia K; Okusa MD. Ultrasound contrast agents in the study of kidney function in health and disease. Drug Discovery Today: Dis. Mech 2007, 4, 153–158.

(18). Unnikrishnan S; Klibanov AL. Microbubbles as ultrasound contrast agents for molecular imaging: preparation and application. Am. J. Roentgenol 2012, 199, 292–299. [PubMed: 22826389]

(19). Sen T; Tufekcioglu O; Koza Y. Mechanical index. Anatol. J. Cardiol 2015, 15, 334. [PubMed: 25880292]

(20). Packer D; Asirvatham S; Monahan K; Shen W; Rea R; Hammill S Progression of Pulmonary Vein Stenosis in Patients Following Focal Atrial Fibrillation Ablation, Circulation; LIPPINCOTT WILLIAMS & WILKINS: 530 WALNUT ST, PHILADELPHIA, PA 19106–3621 USA, 2001; pp 461.

(21). Kanoulas E; Butler M; Rowley C; Voulgaridou V; Diamantis K; Duncan WC; McNeilly A; Averkiou M; Wijkstra H; Mischi M; Wilson RS; Lu W; Sboros V. Super-resolution contrast-enhanced ultrasound methodology for the identification of in vivo vascular dynamics in 2D. Invest. Radiol 2019, 54, 500. [PubMed: 31058661]

(22). Duan J; Zhong H; Jing B; Zhang S; Wan M. Increasing axial resolution of ultrasonic imaging with a joint sparse representation model. IEEE Trans. Ultrason. Ferroelectrics Freq. Control 2016, 63, 2045–2056.

(23). Cho K; Wang X; Nie S; Chen DM; Shin DMTherapeutic nanoparticles for drug delivery in cancer. Clin. Cancer Res 2008, 14, 1310–1316. [PubMed: 18316549]

(24). Wang C; Li J; Amatore C; Chen Y; Jiang H; Wang XM. Gold nanoclusters and graphene nanocomposites for drug delivery and imaging of cancer cells. Angew. Chem 2011, 123, 11848–11852.

(25). Mitchell MJ; Billingsley MM; Haley RM; Wechsler ME; Peppas NA; Langer R Engineering precision nanoparticles for drug delivery. Nat. Rev. Drug Discovery 2021, 20, 101–124. [PubMed: 33277608]

(26). Harish V; Tewari D; Gaur M; Yadav AB; Swaroop S; Bechelany M; Barhoum A. Review on Nanoparticles and Nanostructured Materials: Bioimaging, Biosensing, Drug Delivery, Tissue Engineering, Antimicrobial, and Agro-Food Applications. Nanomaterials 2022, 12, 457. [PubMed: 35159802]

(27). Ashrafzadeh Afshar EA; Taher MA; Karimi-Maleh H; Karaman C; Joo S-W; Vasseghian Y. Magnetic nanoparticles based on cerium MOF supported on the MWCNT as a fluorescence quenching sensor for determination of 6-mercaptopurine. Environ. Pollut 2022, 305, 119230.

(28). Sajjadi M; Nasrollahzadeh M; Jaleh B; Soufi GJ; Iravani S. Carbon-based nanomaterials for targeted cancer nanotherapy: Recent trends and future prospects. J. Drug Targeting 2021, 29, 716–741.

(29). He Y; Hu C; Li Z; Wu C; Zeng Y; Peng C. Multifunctional carbon nanomaterials for diagnostic applications in infectious diseases and tumors. Mater. Today Bio 2022, 14, 100231.

(30). Kansara V; Shukla R; Flora SJS; Bahadur P; Tiwari S. Graphene quantum dots: Synthesis, optical properties and navigational applications against cancer. Mater. Today Commun 2022, 31, 103359.

(31). Nemati F; Zare-Dorabei R; Hosseini M; Ganjali MR. Fluorescence turn-on sensing of thiamine based on Arginine – functionalized graphene quantum dots (Arg-GQDs): Central composite design for process optimization. Sens. Actuators, B 2018, 255, 2078–2085.

(32). Qi L; Pan T; Ou L; Ye Z; Yu C; Bao B; Wu Z; Cao D; Dai L. Biocompatible nucleus-targeted graphene quantum dots for selective killing of cancer cells via DNA damage. Commun. Biol 2021, 4, 214. [PubMed: 33594275]

(33). Zhang Q; Deng S; Liu J; Zhong X; He J; Chen X; Feng B; Chen Y; Ostrikov K. Cancer-targeting graphene quantum dots: fluorescence quantum yields, stability, and cell selectivity. Adv. Funct. Mater 2019, 29, 1805860.

(34). Campbell E; Hasan MT; Gonzalez-Rodriguez R; Truly T; Lee BH; Green KN; Akkaraju G; Naumov AV. Graphene quantum dot formulation for cancer imaging and redox-based drug delivery. Nanomedicine 2021, 37, 102408.

(35). Hai X; Wang Y; Hao X; Chen X; Wang J. Folic acid encapsulated graphene quantum dots for ratiometric pH sensing and specific multicolor imaging in living cells. Sens. Actuators, B 2018, 268, 61–69.

(36). Hasan MT; Lee BH; Lin C-W; McDonald-Boyer A; Gonzalez-Rodriguez R; Vasireddy S; Tsedev U; Coffer J; Belcher AM; Naumov AV. Near-infrared emitting graphene quantum dots synthesized from reduced graphene oxide for in vitro/in vivo/ex vivo bioimaging applications. 2D Mater 2021, 8, 035013.

(37). Yan H; Wang Q; Wang J; Shang W; Xiong Z; Zhao L; Sun X; Tian J; Feng S-S; Kang F. Planting graphene quantum dots in PEGylated nanoparticles for enhanced and multimodal in vivo imaging of tumor, 2022. bioRxiv:486000

(38). Li S; Zhou S; Li Y; Li X; Zhu J; Fan L; Yang S. Exceptionally high payload of the IR780 iodide on folic acid-functionalized graphene quantum dots for targeted photothermal therapy. ACS Appl. Mater. Interfaces 2017, 9, 22332–22341. [PubMed: 28643511]

(39). Su X; Chan C; Shi J; Tsang M-K; Pan Y; Cheng C; Gerile O; Yang M. A graphene quantum dot@ Fe3O4@ SiO2 based nanoprobe for drug delivery sensing and dual-modal fluorescence and MRI imaging in cancer cells. Biosens. Bioelectron 2017, 92, 489–495. [PubMed: 27839733]

(40). Xuan Y; Zhang R-Y; Zhang X-S; An J; Cheng K; Li C; Hou X-L; Zhao Y-D. Targeting N-doped graphene quantum dot with high photothermal conversion efficiency for dual-mode imaging and therapy in vitro. Nanotechnology 2018, 29, 355101.

(41). Hasan MT; Gonzalez-Rodriguez R; Ryan C; Faerber N; Coffer JL; Naumov AV. Photo-and electroluminescence from nitrogen-doped and nitrogen–sulfur codoped graphene quantum dots. Adv. Funct. Mater 2018, 28, 1804337.

(42). Hasan MT; Gonzalez-Rodriguez R; Lin CW; Campbell E; Vasireddy S; Tsedev U; Belcher AM; Naumov AV. Rare-earth metal ions doped graphene quantum dots for near-ir in vitro/in vivo/ex vivo imaging applications. Adv. Opt. Mater 2020, 8, 2000897.

(43). Campbell E; Hasan MT; Gonzalez Rodriguez R; Akkaraju GR; Naumov AV. Doped graphene quantum dots for intracellular multicolor imaging and cancer detection. ACS Biomater. Sci. Eng 2019, 5, 4671–4682. [PubMed: 33448839]

(44). Swietach P; Vaughan-Jones RD; Harris AL; Hulikova A. The chemistry, physiology and pathology of pH in cancer. Philos. Trans. R. Soc., B 2014, 369, 20130099.

(45). Zhao C; Song X; Liu Y; Fu Y; Ye L; Wang N; Wang F; Li L; Mohammadniaei M; Zhang M; Zhang Q; Liu J. Synthesis of graphene quantum dots and their applications in drug delivery. J. Nanobiotechnol 2020, 18, 1–32.

(46). Ajgaonkar R; Lee B; Valimukhametova A; Nguyen S; Gonzalez-Rodriguez R; Coffer J; Akkaraju GR; Naumov AV. Detection of Pancreatic Cancer miRNA with Biocompatible Nitrogen-Doped Graphene Quantum Dots. Materials 2022, 15, 5760. [PubMed: 36013894]

(47). Gu F; Hu C; Xia Q; Gong C; Gao S; Chen Z. Aptamer-conjugated multi-walled carbon nanotubes as a new targeted ultrasound contrast agent for the diagnosis of prostate cancer. J. Nanoparticle Res 2018, 20, 303.

(48). Delogu LG; Vidili G; Venturelli E; Ménard-Moyon C; Zoroddu MA; Pilo G; Nicolussi P; Ligios C; Bedognetti D; Sgarrella F; Manetti R; Bianco A. Functionalized multiwalled carbon nanotubes as ultrasound contrast agents. Proc. Natl. Acad. Sci. U.S.A 2012, 109, 16612–16617. [PubMed: 23012426]

(49). Qian X; Han X; Chen Y. Insights into the unique functionality of inorganic micro/nanoparticles for versatile ultrasound theranostics. Biomaterials 2017, 142, 13–30. [PubMed: 28719818]

(50). Casciaro S; Conversano F; Ragusa A; Ada Malvindi MA; Franchini R; Greco A; Pellegrino T; Gigli G. Optimal enhancement configuration of silica nanoparticles for ultrasound imaging and automatic detection at conventional diagnostic frequencies. Invest. Radiol 2010, 45, 715–724. [PubMed: 20562708]

(51). Qi S; Zhang P; Ma M; Yao M; Wu J; Mäkilä E; Salonen J; Ruskoaho H; Xu Y; Santos HA; Zhang H. Cellular Internalization–Induced Aggregation of Porous Silicon Nanoparticles for Ultrasound Imaging and Protein-Mediated Protection of Stem Cells. Small 2019, 15, 1804332.

(52). Tamarov K; Sviridov A; Xu W; Malo M; Andreev V; Timoshenko V; Lehto V-P. Nano air seeds trapped in mesoporous janus nanoparticles facilitate cavitation and enhance ultrasound imaging. ACS Appl. Mater. Interfaces 2017, 9, 35234–35243. [PubMed: 28921952]

(53). Zhang K; Chen H; Guo X; Zhang D; Zheng Y; Zheng H; Shi J. Double-scattering/reflection in a single nanoparticle for intensified ultrasound imaging. Sci. Rep 2015, 5, 1–11.

(54). Guo M; Du W; Lyu N; Chen X; Du Y; Wang H; Yang D; Wu S; Liang J; Pan Y; Tang D. Ultra-Early Diagnosis of Acute Myocardial Infarction in Rats Using Ultrasound Imaging of Hollow Double-Layer Silica Nanospheres. Adv. Healthcare Mater 2020, 9, 1901155.

(55). Liberman A; Wang J; Lu N; Viveros RD; Allen C; Mattrey R; Blair S; Trogler W; Kim M; Kummel A. Mechanically tunable hollow silica ultrathin nanoshells for ultrasound contrast agents. Adv. Funct. Mater 2015, 25, 4049–4057. [PubMed: 26955300]

(56). Yildirim A; Chattaraj R; Blum NT; Goldscheitter GM; Goodwin AP. Stable encapsulation of air in mesoporous silica nanoparticles: fluorocarbon-free nanoscale ultrasound contrast agents. Adv. Healthcare Mater 2016, 5, 1290–1298.

(57). Gao S; Wang G; Qin Z; Wang X; Zhao G; Ma Q; Zhu L. Oxygen-generating hybrid nanoparticles to enhance fluorescent/photoacoustic/ultrasound imaging guided tumor photodynamic therapy. Biomaterials 2017, 112, 324–335. [PubMed: 27776285]

(58). Kumari A; Singh AK. Use of Solid Nanoparticles as Contrast Agent for Ultrasound Imaging. J. Sci. Tech. Res 2018, 8, 1–4.

(59). Sukumar UK; Natarajan A; Massoud TF; Paulmurugan R Applications of Fluorescent Protein-Based Sensors in Bioimaging. Fluorescent Imaging in Medicinal Chemistry; Springer, 2019; pp 149–183.

(60). Bhavane R; Starosolski Z; Stupin I; Ghaghada KB; Annapragada A. NIR-II fluorescence imaging using indocyanine green nanoparticles. Sci. Rep 2018, 8, 1–10. [PubMed: 29311619]

(61). Nißler R; Kurth L; Li H; Spreinat A; Kuhlemann I; Flavel BS; Kruss S. Sensing with chirality-pure near-infrared fluorescent carbon nanotubes. Anal. Chem 2021, 93, 6446–6455. [PubMed: 33830740]

(62). Hong G; Diao S; Chang J; Antaris AL; Chen C; Zhang B; Zhao S; Atochin DN; Huang PL; Andreasson KI; Kuo CJ; Dai H. Through-skull fluorescence imaging of the brain in a new near-infrared window. Nat. Photonics 2014, 8, 723–730. [PubMed: 27642366]

(63). Kotcherlakota R; Nimushakavi S; Roy A; Yadavalli HC; Mukherjee S; Haque S; Patra CR. Biosynthesized gold nanoparticles: in vivo study of near-infrared fluorescence (NIR)-based bio-imaging and cell labeling applications. ACS Biomater. Sci. Eng 2019, 5, 5439–5452. [PubMed: 33464064]

(64). Chakraborty A; Jana NR. Clathrin to lipid raft-endocytosis via controlled surface chemistry and efficient perinuclear targeting of nanoparticle. J. Phys. Chem. Lett 2015, 6, 3688–3697. [PubMed: 26722743]

(65). Chen T; Li M; Liu J. π–π stacking interaction: a nondestructive and facile means in material engineering for bioapplications. Cryst. Growth Des 2018, 18, 2765–2783.

(66). Biswas MC; Islam MT; Nandy PK; Hossain MM. Graphene quantum dots (GQDs) for bioimaging and drug delivery applications: a review. ACS Mater. Lett 2021, 3, 889–911.

(67). Rasamani KD; Alimohammadi F; Sun Y. Interlayer-expanded MoS 2. Mater. Today 2017, 20, 83–91.

(68). Chen J; Patil S; Seal S; McGinnis JF. Rare earth nanoparticles prevent retinal degeneration induced by intracellular peroxides. Nat. Nanotechnol 2006, 1, 142–150. [PubMed: 18654167]

(69). Tarnuzzer RW; Colon J; Patil S; Seal S. Vacancy engineered ceria nanostructures for protection from radiation-induced cellular damage. Nano Lett 2005, 5, 2573–2577. [PubMed: 16351218]

(70). Gu J; Zhang X; Pang A; Yang J. Facile synthesis and photoluminescence characteristics of blue-emitting nitrogen-doped graphene quantum dots. Nanotechnology 2016, 27, 165704.

(71). Ben Aoun S. Nanostructured carbon electrode modified with N-doped graphene quantum dots–chitosan nanocomposite: a sensitive electrochemical dopamine sensor. R. Soc. Open Sci 2017, 4, 171199.

(72). Mahdavi M; Kimiagar S; Abrinaei F. Preparation of few-layered wide bandgap MoS2 with nanometer lateral dimensions by applying laser irradiation. Crystals 2020, 10, 164.

(73). Hemmer E; Benayas A; Légaré F; Vetrone F. Exploiting the biological windows: current perspectives on fluorescent bioprobes emitting above 1000 nm. Nanoscale Horiz 2016, 1, 168–184. [PubMed: 32260620]

(74). Hasan MT; Gonzalez-Rodriguez R; Ryan C; Coffer JL; Naumov AV. Variation of optical properties of nitrogen-doped graphene quantum dots with short/mid/long-wave ultraviolet for the development of the uv photodetector. ACS Appl. Mater. Interfaces 2019, 11, 39035–39045. [PubMed: 31553149]

(75). Hasan MT; Senger BJ; Mulford P; Ryan C; Doan H; Gryczynski Z; Naumov AV. Modifying optical properties of reduced/graphene oxide with controlled ozone and thermal treatment in aqueous suspensions. Nanotechnology 2017, 28, 065705.

(76). Hasan MT; Senger BJ; Ryan C; Culp M; Gonzalez-Rodriguez R; Coffer JL; Naumov AV. Optical band gap alteration of graphene oxide via ozone treatment. Sci. Rep 2017, 7, 6411. [PubMed: 28743864]

(77). Lyubutin I; Baskakov A; Starchikov S; Shih K-Y; Lin C-R; Tseng Y-T; Yang S-S; Han Z-Y; Ogarkova YL; Nikolaichik V; Avilov AS. Synthesis and characterization of graphene modified by iron oxide nanoparticles. Mater. Chem. Phys 2018, 219, 411–420.

(78). Gonzalez-Rodriguez R; Campbell E; Naumov A. Multifunctional graphene oxide/iron oxide nanoparticles for magnetic targeted drug delivery dual magnetic resonance/fluorescence imaging and cancer sensing. PLoS One 2019, 14, No. e0217072.

(79). Kaur J; Singh M; Dell'Aversana C; Benedetti R; Giardina P; Rossi M; Valadan M; Vergara A; Cutarelli A; Montone AMI; Altucci L; Corrado F; Nebbioso A; Altucci C. Biological interactions of biocompatible and water-dispersed MoS2 nanosheets with bacteria and human cells. Sci. Rep 2018, 8, 1–15. [PubMed: 29311619]

(80). Allan PL; Baxter GM; Weston MJ Clinical Ultrasound: Expert Consult: Online and Print; Elsevier Health Sciences, 2011.

(81). Tu J; Zhang H; Yu J; Liufu C; Chen Z. Ultrasound-mediated microbubble destruction: a new method in cancer immunotherapy. OncoTargets Ther 2018, 11, 5763.

(82). Cao H; Tan Z; Lu M-H; Ji G; Yan X-J; Di C; Yuan M; Guo Q; Su Y; Addad A; Li Z; Xiong D-B. Graphene interlayer for enhanced interface thermal conductance in metal matrix composites: An approach beyond surface metallization and matrix alloying. Carbon 2019, 150, 60–68.

(83). Belova V; Shchukin DG; Gorin DA; Kopyshev A; Möhwald H. A new approach to nucleation of cavitation bubbles at chemically modified surfaces. Phys. Chem. Chem. Phys 2011, 13, 8015–8023. [PubMed: 21448506]

(84). Jin Q; Lin C-Y; Kang S-T; Chang Y-C; Zheng H; Yang C-M; Yeh C-K. Superhydrophobic silica nanoparticles as ultrasound contrast agents. Ultrason. Sonochem 2017, 36, 262–269. [PubMed: 28069209]

(85). Borkent BM; Gekle S; Prosperetti A; Lohse D. Nucleation threshold and deactivation mechanisms of nanoscopic cavitation nuclei. Phys. Fluids 2009, 21, 102003.
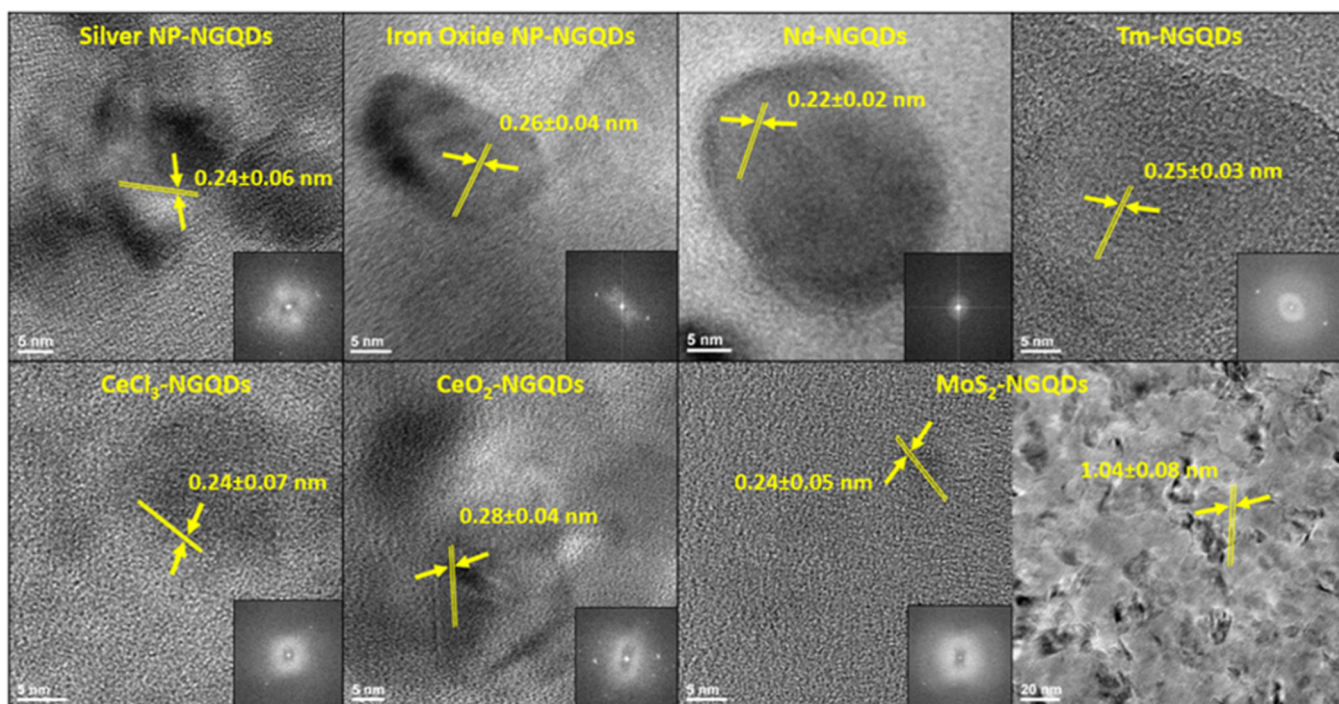
Author Manuscript

Author Manuscript

Author Manuscript

Author Manuscript

Figure 1.
HRTEM images of metal-doped NGQDs with the corresponding interplanar distances. Inset: FFT image of metal-doped NGQDs.
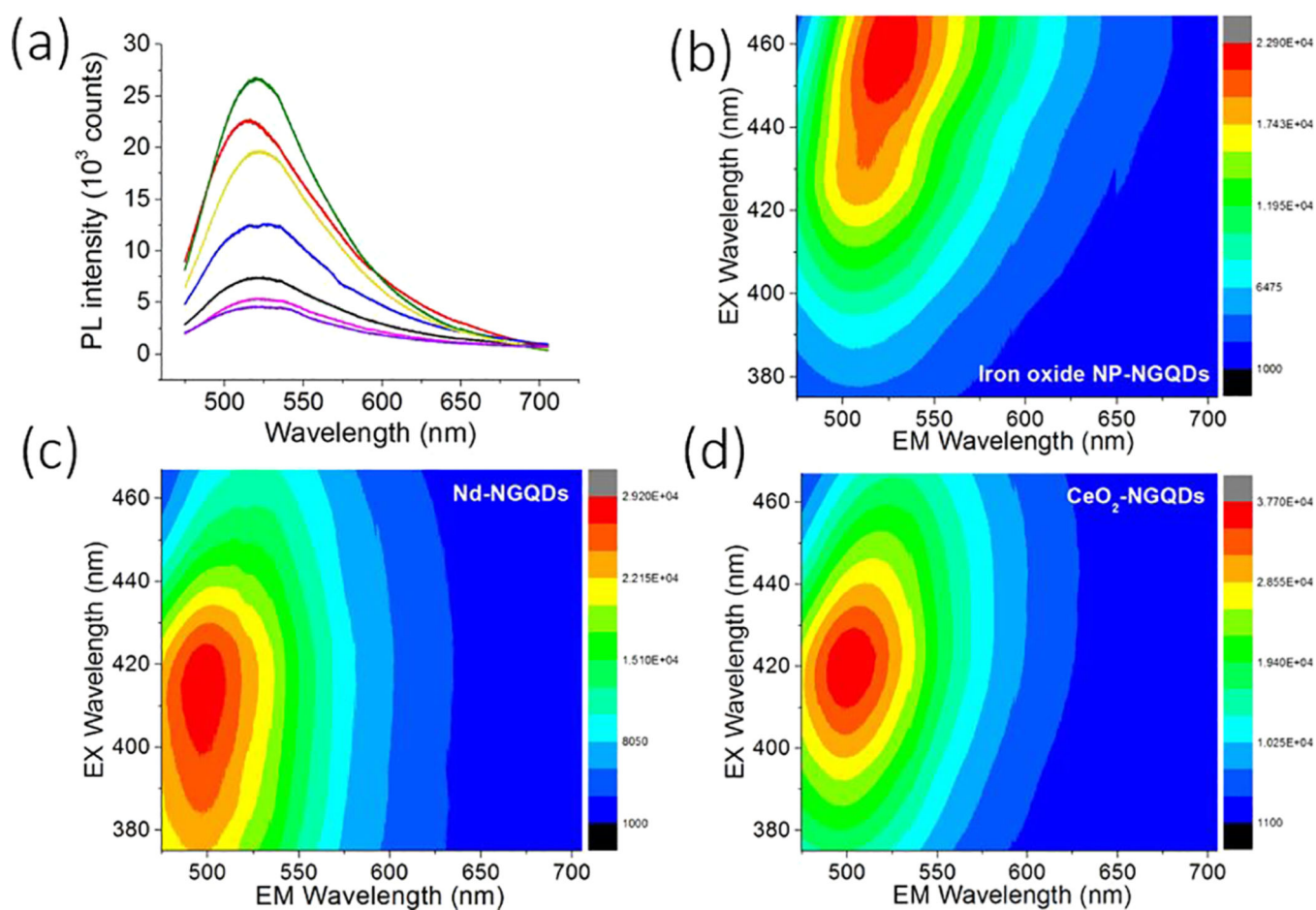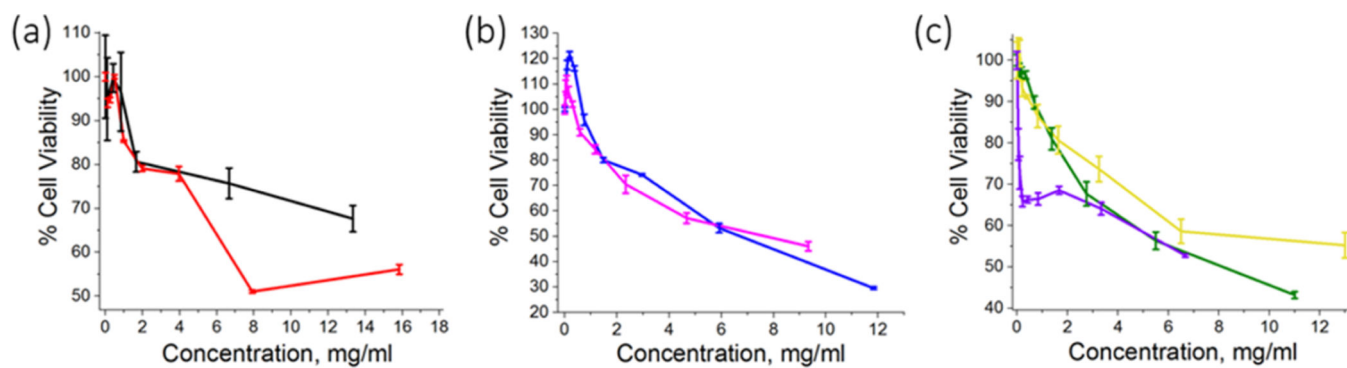
Figure 2.
(a) Fluorescence spectra of samples with 460 nm excitation: $CeCl_3$-NGQDs (green), iron oxide NP-NGQDs (red), CeO_2-NGQDs (yellow), Nd-NGQDs (blue), silver NP-NGQDs (black), Tm-NGQDs (magenta), and MoS_2-NGQDs (violet). Photoluminescence excitation–emission maps of (b) iron oxide NP-NGQDs, (c) Nd-NGQDs, and (d) CeO_2-NGQDs.

Figure 3.
MTT cell viability data for metal-doped NGQDs: (a) silver NP-NGQDs (black) and iron oxide NP-NGQDs (red); (b) Nd-NGQDs (blue) and Tm-NGQDs (magenta); (c) CeCl$_3$-NGQDs (green), CeO$_2$-NGQDs (yellow), and MoS$_2$-NGQDs (violet).
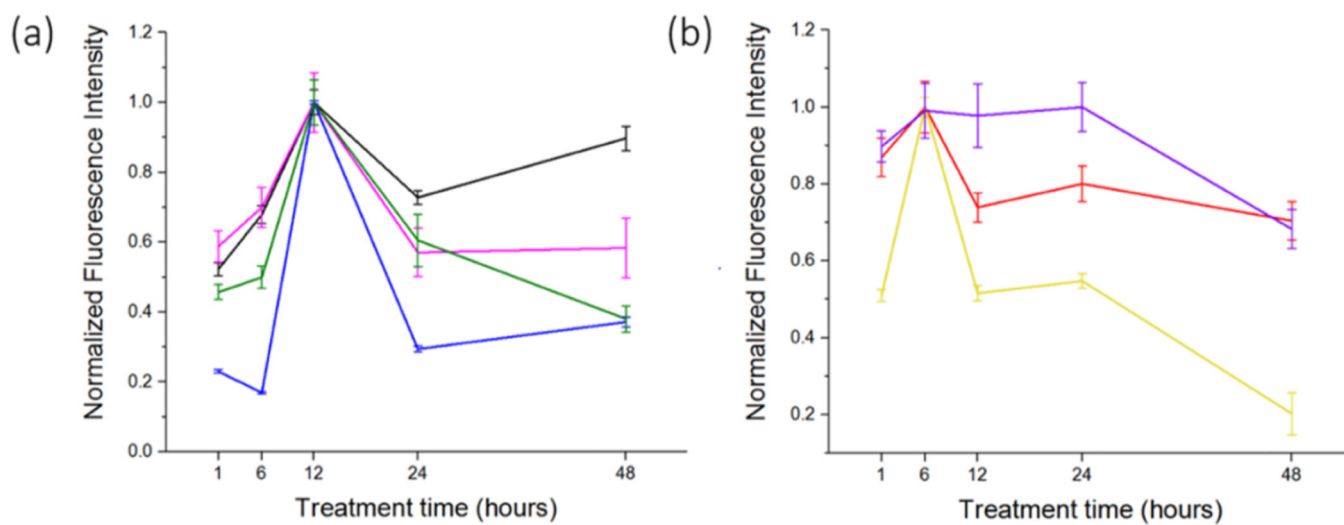
Figure 4.
Cellular internalization/excretion dynamics of all doped NGQD samples over 1, 6, 12, 24, and 48 h based on the fluorescence intensity of NGQDs within the HEK-293 cells (Table S1). (a) Silver NP-NGQDs (black), Nd-NGQDs (blue), Tm-NGQDs (magenta), and $CeCl_3$-NGQDs (green); (b) iron oxide NP-NGQDs (red), CeO_2-NGQDs (yellow), and MoS_2-NGQDs (violet).
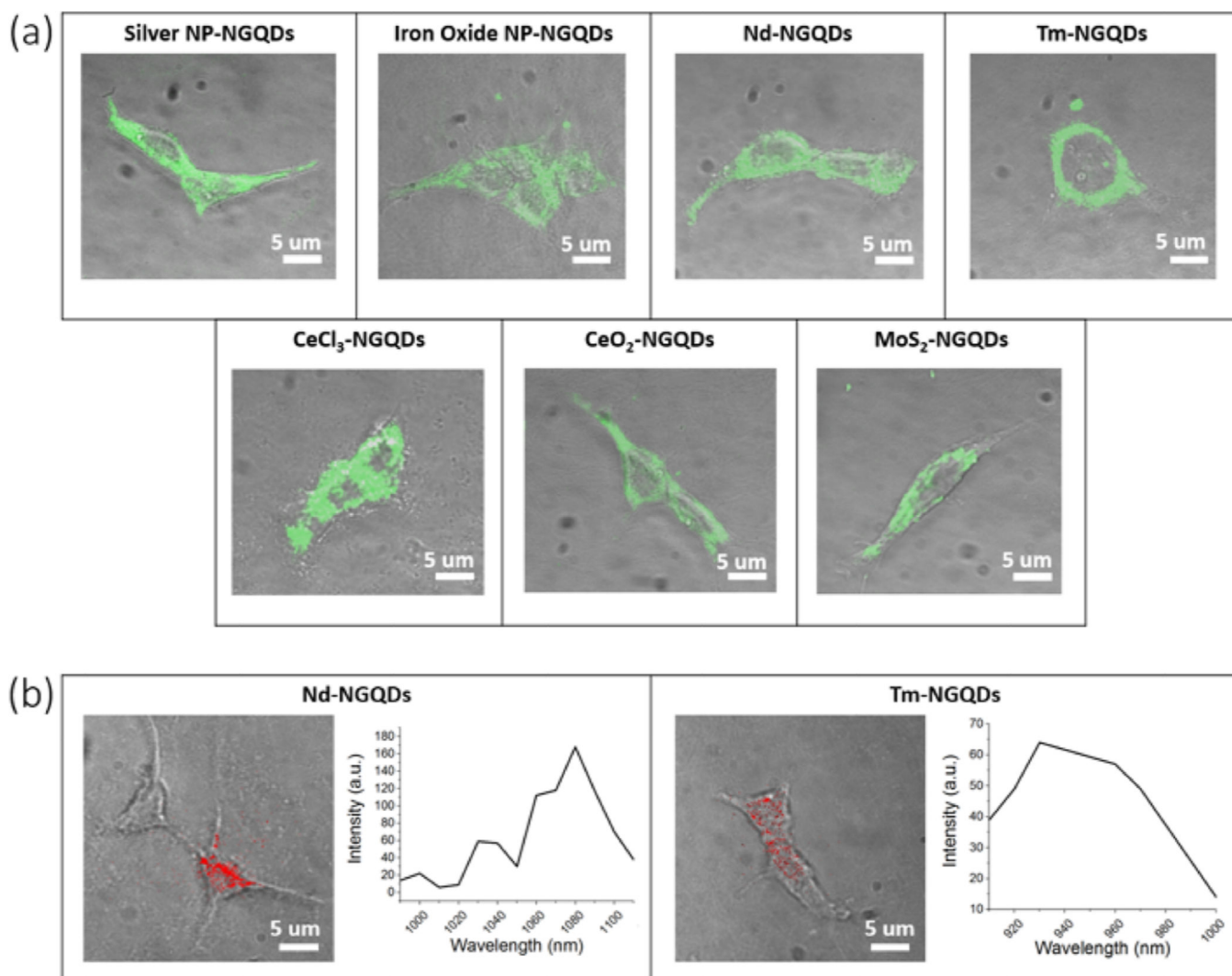
Figure 5.
(a) Bright-field/VIS fluorescence confocal overlay images of HEK-293 cells treated with metal-doped NGQD samples at their optimal internalization time point of 6 (iron oxide NP-NGQDs, CeO_2-NGQDs, and MoS_2-NGQDs) or 12 (silver NP-NGQDs, Nd-NGQDs, Tm-NGQDs, and $CeCl_3$-NGQDs) hours. (b) Bright-field/NIR fluorescence confocal overlay images of HEK-293 cells treated with Nd-NGQD and Tm-NGQD samples for 12 h. Inset: spectra recovered from bright Nd and Tm emission spots within the Nd-NGQDs and Tm-NGQDs-treated samples after background subtraction. Concentration of all NGQDs is 1 mg/mL.
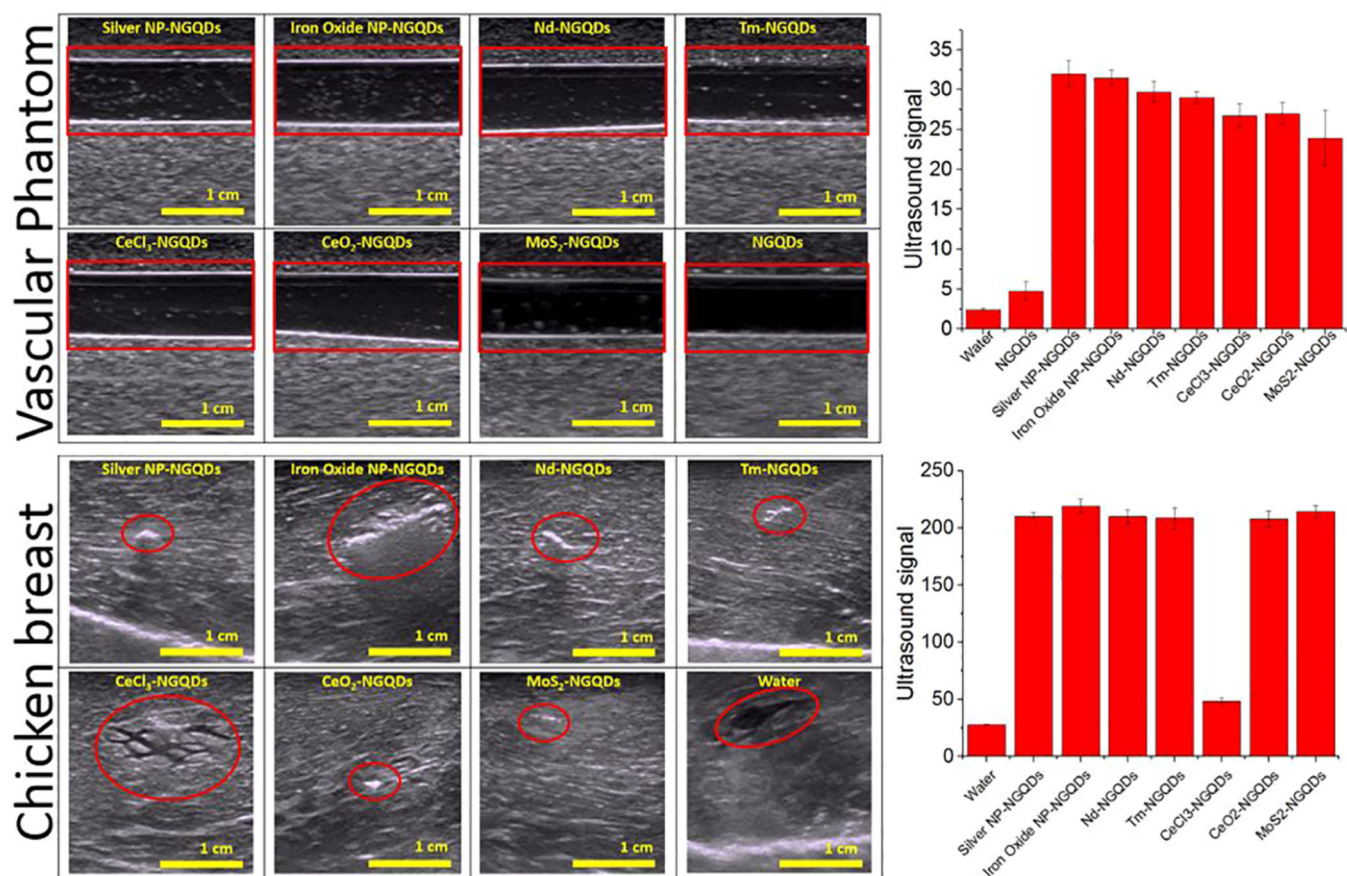
Figure 6.
Ultrasound images of metal-doped NGQDs in the vascular phantom and chicken breast after injection. Bar plots represent the ultrasound signal per unit area in the red-outlined vascular phantom and chicken breast tissue regions, respectively.

Table 1.

Atomic Percentages of Elements in Doped NGQD Samples from EDX Spectra

sample	C	N	O	Cl	Ag	Fe	Nd	Tm	Ce	S	Mo
silver NP-NGQDs	96.94	1.15	1.83	0.03	0.05						
iron oxide NP-NGQDs	94.83	0.72	4.25	0.07		0.13					
Nd-NGQDs[42]	89.99	4.67	4.73				0.61				
Tm-NGQDs[42]	93.51	1.12	4.88					0.48			
CeCl₃-NGQDs	55.14	5.56	21.13	13.58					4.59		
CeO₂-NGQDs	93.66	0.43	5.62	0.04					0.24		
MoS₂-NGQDs	95.06	2.30	2.59							0.04	0.01

atomic percentage, %